

Resolving the Paradox of Oceanic Large-Scale Balance and Small-Scale Mixing

R. Marino,^{1,2,3} A. Pouquet,^{4,1} and D. Rosenberg⁵

¹National Center for Atmospheric Research, P.O. Box 3000, Boulder, Colorado 80307, USA

²Space Sciences Laboratory, University of California, Berkeley, California 94720, USA

³Institute for Chemical-Physical Processes—IPCF/CNR, Rende (CS) 87036, Italy

⁴Laboratory for Atmospheric and Space Physics, University of Colorado at Boulder, Boulder, Colorado 80309, USA

⁵National Center for Computational Sciences, Oak Ridge National Laboratory, P.O. Box 2008, Oak Ridge, Tennessee 37831, USA

(Received 28 September 2014; revised manuscript received 30 December 2014; published 18 March 2015)

A puzzle of oceanic dynamics is the contrast between the observed geostrophic balance, involving gravity, pressure gradient, and Coriolis forces, and the necessary turbulent transport: in the former case, energy flows to large scales, leading to spectral condensation, whereas in the latter, it is transferred to small scales, where dissipation prevails. The known bidirectional constant-flux energy cascade maintaining both geostrophic balance and mixing tends towards flux equilibration as turbulence strengthens, contradicting models and recent observations which find a dominant large-scale flux. Analyzing a large ensemble of high-resolution direct numerical simulations of the Boussinesq equations in the presence of rotation and no salinity, we show that the ratio of the dual energy flux to large *and* to small scales agrees with observations, and we predict that it scales with the inverse of the Froude and Rossby numbers when stratification is (realistically) stronger than rotation. Furthermore, we show that the kinetic and potential energies separately undergo a bidirectional transfer to larger and smaller scales. Altogether, this allows for small-scale mixing which drives the global oceanic circulation and will thus potentially lead to more accurate modeling of climate dynamics.

DOI: 10.1103/PhysRevLett.114.114504

PACS numbers: 47.55.Hd, 47.27.ek, 47.32.Ef

Solar heating, tides, and wind stresses are global-scale energy inputs [1], while in the Southern Ocean, topographic gravity waves provide a small-scale source [2], contributing roughly 50% of its energy [3]. The global ocean acts in a coherent, though complex, fashion from the planetary to the dissipation scale $\approx 1\text{mm}$, with different phenomena interacting like inertia-gravity waves and nonlinear structures such as eddies, zonal jets [4], or fronts [5]. It is known that inverse and direct cascades, respectively, to large and small scales as observed in geophysical fluids [6] and heliospheric plasmas [7,8] can coexist in the purely rotating case [9], as well as in oceanic models [10]. It was shown recently that a dual constant-flux cascade of energy to both large scales and small scales occurs in rotating stratified turbulence (RST) [11]. Moreover, the ratio $R_{\Pi} = |\epsilon_L/\epsilon_s|$ of the total energy fluxes to large and small scales ϵ_L and ϵ_s tends to unity as turbulence becomes dominant as is the case in geophysical and astrophysical fluid dynamics [11]. However, recent studies using altimeter data analyzing sea-surface height in the Southern Ocean, sea-surface height being a proxy for the horizontal velocity field of near-surface currents, and numerical modeling introducing a positive eddy viscosity to represent the effect of the direct energy cascade, show that R_{Π} remains typically between the values 3 and 7 [12,13].

What is the origin of this discrepancy? To answer this question we develop a simple model and conduct an unprecedented study of this problem by means of high-resolution direct numerical simulations (DNS) of the

rotating stably stratified Boussinesq equations. Altogether, 26 runs were performed, 6 on grids of 2048^3 points and 20 on grids of 1024^3 points. Rotation plays an essential role in the building-up of large scales, e.g., through vortex mergers. However, for purely stratified flows, this phenomenon disappears and sharp vertical gradients develop instead. In RST, the disappearance of the inverse cascade, diagnosed through the absence of energy growth in time, appears for large N/f [14–16], which is thus a key parameter varying widely, from ≈ 10 or less in the abyssal Southern Ocean at midlatitude to ≈ 100 or more in the stratosphere; N is the Brunt-Väisälä frequency of gravity waves and $f = 2\Omega$ that of inertial waves, Ω being the rotation rate.

Equations.—We integrate the Boussinesq equations for an incompressible velocity field \mathbf{u} , with $\nabla \cdot \mathbf{u} = 0$:

$$\frac{\partial \mathbf{u}}{\partial t} + N\theta \hat{\mathbf{z}} + f \hat{\mathbf{z}} \times \mathbf{u} - \nu \nabla^2 \mathbf{u} - \mathbf{F}_v = -\nabla p - \mathbf{u} \cdot \nabla \mathbf{u}, \quad (1)$$

$$\frac{\partial \theta}{\partial t} - N \mathbf{u} \cdot \hat{\mathbf{z}} - \kappa \nabla^2 \theta = -\mathbf{u} \cdot \nabla \theta. \quad (2)$$

θ represents temperature (or density) fluctuations. With $\partial_z \bar{\theta}$ the background imposed stratification, $N = \sqrt{-g \partial_z \bar{\theta} / \theta_0}$; p is the pressure normalized to a unit mass density, and $\text{Pr} = \nu/\kappa$ is the Prandtl number, with ν the kinematic viscosity and κ the diffusivity. We take $\text{Pr} = 1$, as suggested by the framework of the renormalization group [17].

The other dimensionless parameters are the Reynolds, Rossby, and Froude numbers and the buoyancy Reynolds:

$$\text{Re} = \frac{U_0 L_F}{\nu}, \quad \text{Ro} = \frac{U_0}{L_F f}, \quad \text{Fr} = \frac{U_0}{L_F N}, \quad \mathcal{R}_B = \text{ReFr}^2, \quad (3)$$

with U_0 and L_F characteristic velocity and length scales. The momentum forcing \mathbf{F}_v is random, three dimensional, and isotropic; it is applied in the shells $k_F = 2\pi/L_F \in (10, 11)$ for all runs but one, for which $k_F \in (7, 8)$. The equations are solved in a triply periodic cubic domain of 2π dimension with n_p^3 points; time evolution is done with a second-order Runge-Kutta scheme, and we use the Geophysical High-Order Suite for Turbulence (GHOST) hybrid-parallelized code [18]. In the ocean, salinity and temperature contribute to density variations; mixing is due to a combination of shear instability, gravity-wave steepening, and double diffusion leading to salt fingering [19], but the convective instability itself may not be the main feature when compared to baroclinic instabilities. Thus, as a first step in our study, salinity is not included. Taking the Fourier transform of Eq. (2), one defines the kinetic isotropic energy flux:

$$\Pi_V(k) = \int_{k_{\min}}^k T_V(q) dq, \quad T_V(q) = -\sum_{C_q} \hat{\mathbf{u}}_q^* \cdot (\mathbf{u} \cdot \widehat{\nabla} \mathbf{u})_q$$

with C_q the shell $q \leq |\mathbf{q}| < q+1$; $\Pi_P = -d_t E_P$ is computed in a similar way. The total flux is $\Pi = \Pi_V + \Pi_P$, with $\int_0^k \Pi(p) dp = -d_t E$.

A dual constant-flux energy cascade.—The development of both large and small scales in RST flows can be observed on the vertical vorticity field $[\omega_z = \nabla \times \mathbf{v}] \cdot \hat{e}_z$ shown in Fig. 1(a) (with \hat{e}_z the unit vector in the vertical direction, collinear with rotation and gravity), as well as on the vertical velocity [11]. The snapshot in Fig. 1(a) is for a flow on grid of 2048^3 points $N/f = 10.5$, $\text{Re} \approx 2 \times 10^4$, and $\text{Fr} \approx 0.047$. The simultaneous presence of small-scale and large-scale features can be diagnosed on the temporal evolution of the integral scales $L_{\text{int}}^X = \int [E_X(k)/k] dk / \int E_X(k) dk$, with $X = V$ or $X = P$, displayed in Fig. 1(b) and associated with the kinetic and potential energy spectra $E_{V,P}(k)$. In a three-dimensional turbulent flow, L_{int}^V grows slowly with time [6]. Here, the scale associated with velocity fluctuations L_{int}^V grows quasilinearly, typical of vortex mergers, whereas L_{int}^P has a slower growth (see also Ref. [20]). We show in Fig. 2(a) the kinetic isotropic energy spectrum at the final time of a run with $N/f = 7$ and $t/\tau_{\text{NL}} = 29$, where $\tau_{\text{NL}} = L_F/U_0$ is the turnover time; it is compensated either by $\alpha \epsilon_V^{2/3} k^{-5/3}$ or by $\alpha \epsilon_V^{2/3} k^{-2.5}$, with $\epsilon_V = \langle \mathbf{u} \cdot \mathbf{F}_v \rangle$ and α being a proportionality constant. Two ranges clearly appear, separated by k_F . The large-scale inertial index corresponds to that of the

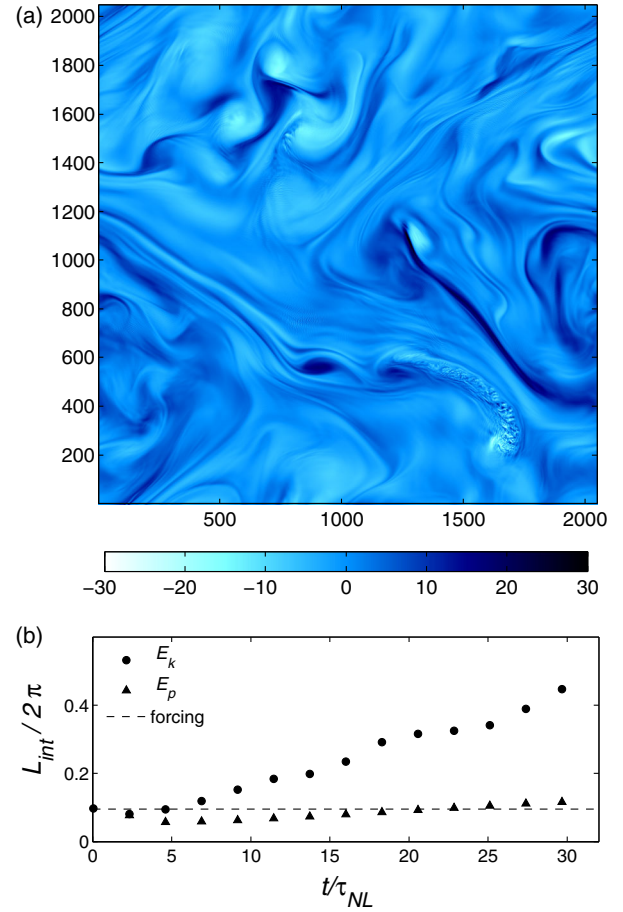


FIG. 1 (color online). (a) Horizontal cut of vertical vorticity: one observes large-scale filaments and small-scale gradients, together with intense localized vortex streets as seen, e.g., for $x = 1700$ and $y = 300$. (b) Time evolution of integral scales based on velocity (circles) and temperature (triangles) for the same run. After an initial transient phase, the former grows significantly in time, while the latter has a slow growth.

inverse cascade of energy in two-dimensional flows [26], and the Kolmogorov constant, read from the vertical axis of Fig. 2(a), is $C' \approx 10$, close to the classic case of 2D turbulence, for which $C' \approx 7$ is found [27].

The small-scale spectrum is steep, as seen in numerous computations [28–30] and oceanic observations [13,31]. It is argued in Ref. [31] that these variations are compatible with the weak-turbulence theory for such flows. The inset gives the temporal variation of the scaled dissipation and kinetic energy for that run, with an energy growth typical of inverse cascades.

Scaling model for the energy-flux ratio.—One observes different spectra in the wave-turbulence regime, the cascade rate to small scales being smaller the smaller the Froude number. This can be seen through a simple dimensional argument, when modeling the slowing-down of nonlinear interactions in the presence of waves, by stating that the transfer time of energy is longer than the turnover time τ_{NL} as $\tau_{\text{tr}} = \tau_{\text{NL}} \times \text{Fr}^a$, $a < 0$; thus, $\epsilon_s = \epsilon_K \times \text{Fr}^{-a}$, where

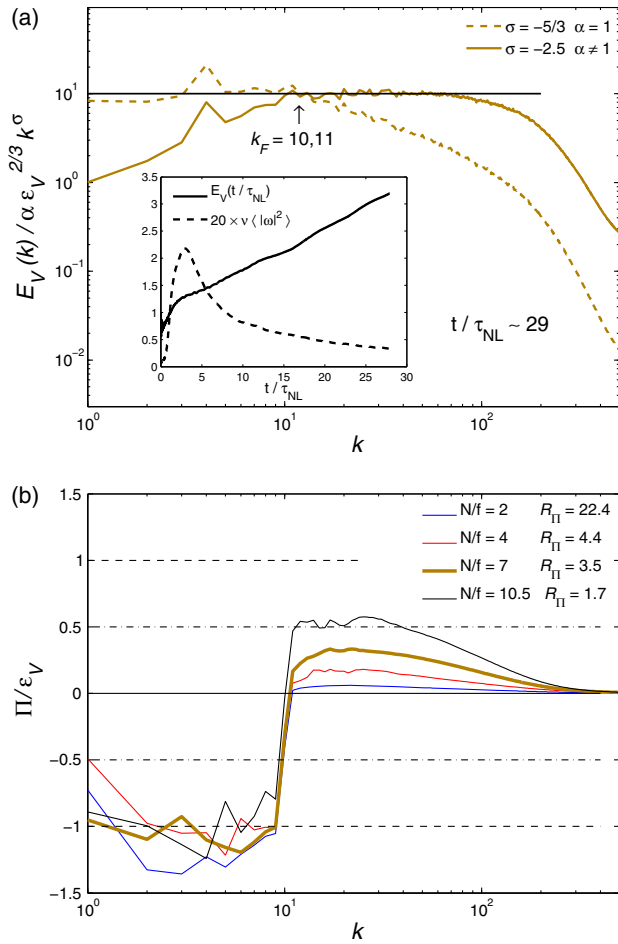


FIG. 2 (color online). (a) Compensated kinetic energy spectra with (in the inset) the time evolution of kinetic energy (solid line) and of its (normalized) dissipation (dashed line); $30\tau_{\text{NL}} \approx 600^+ N^{-1}$ for $\text{Fr} \approx 0.047$, $N/f = 7$, and $\text{Re} \approx 2 \times 10^4$. The large scales follow a $\sim k^{-5/3}$ spectrum, whereas at small scales, $E_V(k) \sim k^{-2.5}$; the spectra cross at $k_F \approx 10.5$. (b) Total energy flux, normalized by $\epsilon_V = \langle \mathbf{u} \cdot \mathbf{F}_v \rangle$, for $2 \leq N/f \leq 10.5$ and runs with similar Froude and Reynolds numbers ($0.045 \leq \text{Fr} \leq 0.047$, $\text{Re} \approx 2 \times 10^4$).

$\epsilon_K = E_V/\tau_{\text{NL}} = U_0^3/L_F$ is the energy transfer rate for homogeneous isotropic turbulence. Indeed, we know that in wave turbulence, the small-scale flux is diminished, compared to ϵ_K in proportion to the relative strength of the waves, with $a = -1$ at lowest order in the expansion, corresponding to three-wave resonances. This argument is compatible with the energy spectra for the purely rotating case [32,33]. Similarly, one can argue that at fixed stratification, the cascade rate to small scales is weaker for stronger rotation.

However, the direct cascade of energy in RST is likely dominated by stratification, following, e.g., the argument in Ref. [34] that strong gradients develop in the vertical so that the Froude number based on a vertical length scale is of order one. On the other hand, one expects that the larger the rotation, the more efficient the inverse cascade is, compared

to the direct cascade rate, irrespective of the strength of the latter, so that at fixed stratification, $R_{\text{II}} \sim \text{Ro}_{\text{Fr}}^b$, $b < 0$ (see also Ref. [9]). Indeed, in the presence of rotation, however weak (but still with $\text{Ro} < \text{Ro}_c$, $\text{Ro}_c \approx 1$ being a critical Rossby number for the onset of an inverse cascade), there is a channel for the energy to go to larger scales, in a proportion that is greater for stronger rotation. Thus, altogether and assuming for simplicity $a = b$,

$$R_{\text{II}} = |\epsilon_L/\epsilon_s| \sim [\text{Fr} \times \text{Ro}]^{-1}. \quad (4)$$

This phenomenological argument is corroborated by the results of our study, summarized in Fig. 3 in the form of three scatter plots. Each data point represents a run with different parameters in the ranges $2 \leq N/f \leq 10.5$, $0.02 \leq \text{Fr} \leq 0.14$, $0.09 \leq \text{Ro} \leq 0.76$, $6400 \leq \text{Re} \leq 39000$, and $4 \leq \mathcal{R}_B \leq 313$.

The simplest observation stemming from this extensive high-resolution study is that the flux ratio varies substantially. Also, for fixed Froude and Reynolds numbers, and thus fixed \mathcal{R}_B , this ratio varies by 1 order of magnitude [see the legend in Fig. 2(b)], indicating that \mathcal{R}_B is not the determining parameter, provided it is large enough, but that rotation plays an essential role in the energy distribution, even if weak compared to stratification.

Five main trends are detected from these plots. (i) The energy flux to large scales, relative to that to small scales, becomes weaker (although it does not disappear entirely) for larger N/f . (ii) However, for \mathcal{R}_B of order 17 or below (data points with empty symbols), the ratio of fluxes follows an unrelated trend, indicative of a different regime [Fig. 3(a)]; the existence of \mathcal{R}_B -dependent regimes has been advocated by several authors (see, e.g., Ref. [35]); indeed, for $\mathcal{R}_B < 1$, the Ozmidov length scale at which isotropy recovers is smaller than the dissipation scale, and strong turbulence cannot develop. (iii) Setting aside the high values of \mathcal{R}_B for $N/f = 2$ (up to ~ 300), and the values lower than ≈ 17 , the rest of the study is done for $26 \leq \mathcal{R}_B \leq 57$, and in that range, R_{II} displays a variation of 2 orders of magnitude determined by the intrinsic dynamics of the flow, and not \mathcal{R}_B itself. (iv) A transition in the rate of variation of R_{II} with Froude number occurs around $[N/f]_C = 7$ [Fig. 3(b)]. And (v) in roughly one third of the runs, there is a dual energy transfer separately for the kinetic and the potential modes, with negative fluxes at large scales and positive at small scales. This is shown in Fig. 3(c) (inset) where the flux ratio is also plotted individually for E_V and E_p , the former dominating the latter.

In Fig. 3(b) the data are plotted against $\text{Fr} \times \text{Ro}$, as suggested by the preceding phenomenological analysis [Eq. (4)]. One sees that the points are rather well aligned, with a slope close to -1 for moderate values of N/f . For larger N/f , this slope is close to -2 , indicative of two regimes in N/f (see the inset). The origin of this transition

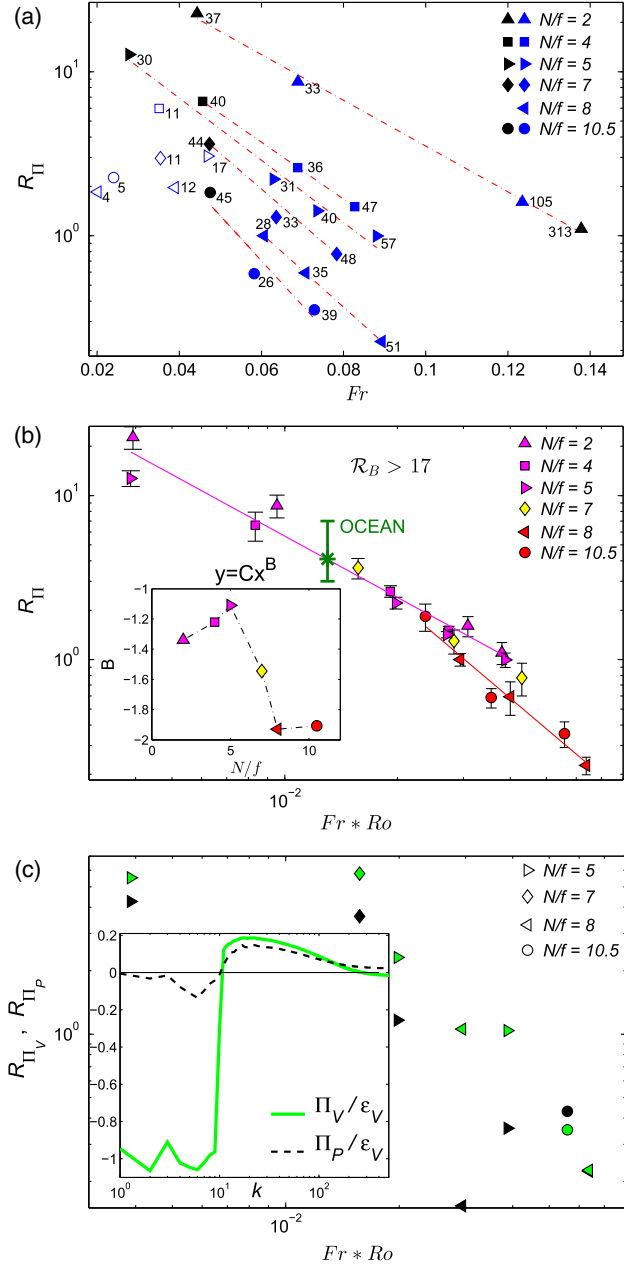


FIG. 3 (color online). Scatter plots of R_{Π} as a function of (a) Fr and (b),(c) $Fr \times Ro$ in lin-log and log-log coordinates, respectively. (a) Points are labeled by their final \mathcal{R}_B ; the six runs with 2048^3 grids have $16500 \leq Re \leq 39000$ (black symbols) while the others use a 1024^3 grid and $6400 \leq Re \leq 10000$ (blue symbols). (b) The six runs with low \mathcal{R}_B shown in (a) with empty symbols are eliminated in (b) and (c); the same symbols are used, but colors now indicate three ranges for N/f . The vertical green bar gives a plausible interval of R_{Π} values for the ocean [12,13]. The inset gives the slope of the variation of R_{Π} with $Fr \times Ro$ for various N/f . Error bars on R_{Π} are based on the standard deviations associated with the averages of the fluxes over about a decade of scales. (c) Scatter plot of the ratio of kinetic energy fluxes (green symbols) or potential energy fluxes (black symbols) $R_{\Pi_{V,P}}$ for flows with a bidirectional energy transfer with negative flux for $k < k_F$ and positive for $k > k_F$. The inset shows energy fluxes for velocity (solid line) and temperature (dashed line), for the same flow as in Fig. 2(a) ($N/f = 7$).

is not clear. There is a known change of regime in N/f , attributed to the lack of resonant interactions in the range $1/2 \leq N/f \leq 2$ [36]. One could argue that higher-order wave terms in a weak-turbulence expansion would involve interactions with more than three waves, thereby inducing a shift in the transitional values of N/f , as well as resonance broadening, and that might induce a shift in the behavior for larger N/f . Another possibility is associated with finite size effects, i.e., to the limited ratio between the forcing scale and the overall size of the flow, or the Rossby deformation radius.

The abyssal Southern Ocean.—This study is done in the general context of the interactions between different types of waves and turbulent eddies and their influence on the overall distribution of energy in RST. When recasting it in the specific context of the abyssal Southern Ocean at midlatitudes, typical parameters are as follows. Lee-wave generation due to bathymetry is known to occur at scales between 200 and 2000 m, with a peak at 800 m [2], so we take $L_F = 450$ m and an overall domain size of 4500 m. The amplitude of the forcing is such that the mean geostrophic wind is $U_0 = 0.02$ m/s (see, e.g., Ref. [3]). Finally, we choose $\nu = 4.5 \times 10^{-4}$ m² s⁻¹, giving $Re = 2 \times 10^4$; this value is imposed by the grid resolution of the DNS and is still low compared to geophysical values. This leads to a (Kolmogorov) energy dissipation rate of $\epsilon_K = U_0^3/L_F \approx 1.8 \times 10^{-8}$ m² s⁻³ per unit mass, comparable to, although larger than, measured values. The Coriolis parameter is chosen as $f = 1.2 \times 10^{-4}$ s⁻¹, and $N = 1.26 \times 10^{-3}$ s⁻¹ as determined by direct measurements, for example, in the Drake passage [3], leading to $N/f \approx 10.5$. Thus, the Froude number is $Fr \approx 0.035$, $\mathcal{R}_B \approx 25$, and the Rossby number is 0.37, large but still leading to the occurrence of an inverse cascade [14]. The value of the flux ratio extrapolated for $Fr = 0.035$ and $Ro = 0.37$ using Fig. 3(b) is ≈ 4.1 (green star), within the bounds of measured values in the ocean (from 3 to 7, as reported in Refs. [12,13]) indicated by the green bar in Fig. 3(b). For these parameters, $Fr \times Ro = 0.013$ and the effective energy dissipation is $\epsilon_W \sim \epsilon_K \times Fr \approx 6.3 \times 10^{-10}$ W. Two effects are likely to be balancing each other in achieving such a reasonable agreement of our simulations with the observations. On the one hand, higher \mathcal{R}_B as found in geophysical flows will likely lead to an equipartition of fluxes [11]. But on the other hand, the fact that the ocean and the atmosphere have a small aspect ratio may weaken the direct cascade as found in Ref. [37]. Thus, above a threshold in \mathcal{R}_B (here found ≈ 17), one enters a generic turbulent regime modulated by waves and depending on a balance between rotation and stratification. This suggests that indeed small-scale dissipation can be parametrized using the estimation of ϵ_W stemming from weak-turbulence phenomenology and/or using measurements of R_{Π} .

Conclusion.—The balance between inverse and direct energy fluxes in rotating stratified flows is found in this

Letter to be close to oceanic values when using realistic parameters in DNS. One can estimate that globally the small-scale dissipation is between 20% and 25% of the available energy, thus alleviating the long-standing issue in ocean and climate dynamics concerning the amount of energy dissipation. Performing modeling of such flows may misrepresent small-scale statistics, as shown, for example, in Ref. [38], but recent numerical experiments at moderate resolution using such a technique [39] do find an inverse cascade of energy for Boussinesq flows. The findings presented herein thus might help devise more realistic turbulence closures for the atmosphere and ocean. This will lead to a better assessment of mixing in the ocean and thus to a better estimation of the global circulation affecting climate dynamics [40].

This work was supported by NSF/CMG/1025183, Regional Operative Program Calabria ESF 2007/2013, and Marie Curie Project FP7PIRSES-2010-269297-Turbo-plasmas. It used resources of the ORNL/OLCF, which is supported by the DOE Office of Science under Contract No. DE-AC05-00OR22725. Computer time was provided by ASD at NCAR, which is supported by NSF.

-
- [1] R. Ferrari and C. Wunsch, *Annu. Rev. Fluid Mech.* **41**, 253 (2009).
- [2] R. B. Scott, J. A. Goff, A. C. Naveira Garabato, and A. J. G. Nurser, *J. Geophys. Res.* **116**, C09029 (2011).
- [3] M. Nikurashin and R. Ferrari, *Geophys. Res. Lett.* **40**, 3133 (2013).
- [4] B. Galperin, H. Nakano, H. P. Huang, and S. Sukoriansky, *Geophys. Res. Lett.* **31**, L13303 (2004).
- [5] E. D'Asaro, C. Lee, L. Rainville, R. Harcourt, and L. Thomas, *Science* **332**, 318 (2011).
- [6] M. Lesieur, *Turbulence In Fluids* (Springer-Verlag, Berlin, 2008).
- [7] R. Marino, L. Sorriso-Valvo, V. Carbone, P. Veltri, A. Noullez, and R. Bruno, *Planet. Space Sci.* **59**, 592 (2011).
- [8] R. Marino, L. Sorriso-Valvo, R. D'Amicis, V. Carbone, R. Bruno, and P. Veltri, *Astrophys. J.* **750**, 41 (2012).
- [9] L. M. Smith, J. R. Chasnov, and F. Waleffe, *Phys. Rev. Lett.* **77**, 2467 (1996).
- [10] P. Klein, B. L. Hua, G. Lapeyre, X. Capet, S. Le Gentil, and H. Sasaki, *J. Phys. Oceanogr.* **38**, 1748 (2008).
- [11] A. Pouquet and R. Marino, *Phys. Rev. Lett.* **111**, 234501 (2013).
- [12] B. Arbic, K. Polzin, R. B. Scott, J. Richman, and J. Shriver, *J. Phys. Oceanogr.* **43**, 283 (2013).
- [13] R. B. Scott and F. Wang, *J. Phys. Oceanogr.* **35**, 1650 (2005).
- [14] M. Waite and P. Bartello, *J. Fluid Mech.* **568**, 89 (2006).
- [15] R. Marino, P. D. Mininni, D. L. Rosenberg, and A. Pouquet, *Europhys. Lett.* **102**, 44006 (2013).
- [16] R. Marino, P. D. Mininni, D. L. Rosenberg, and A. Pouquet, *Phys. Rev. E* **90**, 023018 (2014).
- [17] D. Forster, D. R. Nelson, and M. J. Stephen, *Phys. Rev. Lett.* **36**, 867 (1976).
- [18] P. D. Mininni, D. Rosenberg, R. Reddy, and A. Pouquet, *Parallel Comput.* **37**, 316 (2011).
- [19] W. G. Large, J. C. McWilliams, and S. C. Doney, *Rev. Geophys.* **32**, 363 (1994).
- [20] See Supplemental Material at <http://link.aps.org/supplemental/10.1103/PhysRevLett.114.114504> for a brief spectral analysis of potential energy and kinetic enstrophy, which includes Refs. [12,16,21–25,33,35].
- [21] P. Bartello, *J. Atmos. Sci.* **52**, 4410 (1995).
- [22] C. Herbert, A. Pouquet, and R. Marino, *J. Fluid Mech.* **758**, 374 (2014).
- [23] C. Rorai, P. D. Mininni, and A. Pouquet, *Phys. Rev. E* **89**, 043002 (2014).
- [24] H. Aluie and S. Kurien, *Europhys. Lett.* **96**, 44006 (2011).
- [25] Y. V. Lvov and E. G. Tabak, *Phys. Rev. Lett.* **87**, 168501 (2001).
- [26] R. H. Kraichnan, *Phys. Fluids* **10**, 1417 (1967).
- [27] G. Boffetta and R. Ecke, *Annu. Rev. Fluid Mech.* **44**, 427 (2012).
- [28] J. P. Laval, J. C. McWilliams, and B. Dubrulle, *Phys. Rev. E* **68**, 036308 (2003).
- [29] X. Capet, J. C. McWilliams, M. J. Molemaker, and A. F. Shchepetkin, *J. Phys. Oceanogr.* **38**, 2256 (2008).
- [30] M. Nikurashin, G. K. Vallis, and A. Adcroft, *Nat. Geosci.* **6**, 48 (2012).
- [31] K. Polzin and Y. Lvov, *Rev. Geophys.* **49**, RG4003 (2011).
- [32] P. D. Mininni, D. Rosenberg, and A. Pouquet, *J. Fluid Mech.* **699**, 263 (2012).
- [33] S. Galtier, *Phys. Rev. E* **68**, 015301 (2003).
- [34] P. Billant and J.-M. Chomaz, *Phys. Fluids* **13**, 1645 (2001).
- [35] G. Ivey, K. Winters, and J. Koseff, *Annu. Rev. Fluid Mech.* **40**, 169 (2008).
- [36] L. Smith and F. Waleffe, *J. Fluid Mech.* **451**, 145 (2002).
- [37] E. Deusebio, G. Boffetta, E. Lindborg, and S. Musacchio, *Phys. Rev. E* **90**, 023005 (2014).
- [38] K. Spykma, M. Magcalas, and N. Campbell, *Phys. Fluids* **24**, 125102 (2012).
- [39] A. M. Brunner-Suzuki, M. A. Sundermeyer, and M. P. Lelong, *J. Phys. Oceanogr.* **44**, 2446 (2014).
- [40] A. C. Naveira Garabato, K. L. Polzin, B. A. King, K. J. Heywood, and M. Visbeck, *Science* **303**, 210 (2004).